


The influence of in-cylinder flows and bulk gas density on early Spray G injection in an optical research engine

International J of Engine Research
2023, Vol. 24(1) 82–98
© IMechE 2021
Article reuse guidelines:
sagepub.com/journals-permissions
DOI: 10.1177/14680874211042320
journals.sagepub.com/home/fer


Cooper Welch¹ , Marius Schmidt¹ , Christopher Geschwindner¹ ,
Shengqi Wu², Margaret S Wooldridge³  and Benjamin Böhm¹

Abstract

A well-characterized multi-hole gasoline injector, the Engine Combustion Network's (ECN) *Spray G* injector, was investigated in an optically accessible research engine under four motored operating conditions with early injection. The experiments were conducted at intake pressures of 0.4 bar and 0.95 bar, nearly matching the ECN's standard early injection operating conditions, *Spray G2* (flash boiling) and *Spray G3* (early injection), respectively. This was combined with two engine speeds at 800 rpm and 1500 rpm. Using particle image velocimetry and volumetric Mie scatter imaging, the in-cylinder flows were evaluated and the effects on the spray morphology were characterized. The in-cylinder flow was evaluated to understand the spray-flow interaction, including the turbulent kinetic energy. Little effect on turbulent energy was observed in the region examined near the exit of the fuel injector nozzle shortly after injection. Mie scatter imaging was used to characterize the spray morphology and wall wetting was clearly visible on the spark plug. Cyclic variability of the sprays was found to be insignificant; and major differences in spray morphology are attributed to the in-cylinder velocity and intake pressure at the time of injection. Decreasing the bulk gas density by decreasing the intake pressure had a number of effects on the evolution of the spray including faster evaporation, increased axial liquid penetration, and decreased spray angle. Increasing the in-cylinder flow magnitudes by increasing the engine speed had a similar effect on spray morphology by also increasing the evaporation rate, increasing the axial penetration, and decreasing the spray opening angle. Comparison of the motored spray cases with a no-flow case (when the fuel is sprayed into the engine without the piston present) further illustrated the extent to which the intake flow influenced the spray shape.

Keywords

Direct injection spark-ignition, Spray G, particle image velocimetry, spray-flow interaction

Date received: 19 May 2021; accepted: 7 August 2021

Introduction

In order for passenger cars employing combustion engines to remain a viable option in a quickly changing global mobility transformation, next-generation engines must be designed to meet and exceed stringent emissions regulations. One promising technology for increasing efficiency and decreasing emissions is direct injection spark-ignition (DISI) engines, which offer the advantages of precise control of the amount of fuel injected, the timing of injection, and the location of injection, which in the case of stratified combustion, allows for lean mixtures.¹ While stratified charge spark-ignition (SI) engines offer the advantage of a high specific power output in low load operation, they are plagued by seemingly random misfires and partial

burns resulting from sensitivity to minimal changes in the mixture at the time of ignition^{2,3} as well as a susceptibility of spray impingement on the piston due to late injection timings, leading to increased particulate

¹Department of Mechanical Engineering, Reactive Flows and Diagnostics, Technical University of Darmstadt, Darmstadt, Germany

²School of Aeronautics and Astronautics, Shanghai Jiao Tong University, Shanghai, China

³Departments of Mechanical Engineering and Aerospace Engineering, University of Michigan, Ann Arbor, MI, USA

Corresponding author:

Cooper Welch, Department of Mechanical Engineering, Reactive Flows and Diagnostics, Technical University of Darmstadt, Otto-Berndt-Str. 3, Darmstadt 64287, Germany.
Email: welch@rsm.tu-darmstadt.de

emissions.^{3,4} For the aforementioned reasons, research, and manufacturing of passenger car engines over the last decades has largely shifted from stratified charge, late injection, to homogeneous (stoichiometric), early injection, DISI technology because of the benefits of precise control of the fuel injection, efficient use in full load and speed ranges, charge cooling associated with the evaporation of the fuel in the cylinder, and the effectiveness of the use of three-way catalyst systems with stoichiometric mixtures, which achieve significant reductions in NO_x, CO, and HC emissions.^{1,5}

A recent movement in DISI technology has placed the emphasis not on the design of the engine geometry to facilitate atomization and proper mixing near the spark plug, as in older wall-guided configurations, but on the design of the injector, which itself should achieve the same goals, ideally without wall wetting.¹ These spray-guided engine configurations therefore require careful design of the injector systems and much research and development has to be done to first understand, then optimize the mechanisms involved in efficient DISI combustion.

Even in early injection systems, the mixture preparation processes are much more complex than in port fuel injection because the spray must rapidly evaporate before impingement on in-cylinder surfaces and must properly mix before ignition. Multi-hole nozzles with wide global spray angles⁶ have emerged as a preferred design solution for achieving adequate dispersion and mixing, but the in-cylinder flow motion, usually characterized as a tumble-inducing flow, plays a big role in these processes.¹ However, spray impingement on in-cylinder surfaces remains an important consideration in the design of DISI engines because apart from injector nozzle and cylinder geometry design, recent studies have shown that more factors such as fuel temperature, coolant temperature, injection pressure, injection timing, fuel concentration, and engine load affect fuel film deposition and subsequent particulate emissions due to locally rich combustion.⁷⁻⁹ Therefore, it is crucial to identify wall wetting on all surfaces so that it may be avoided in future implementations.

As mixing and dispersion processes are largely dominated by the in-cylinder motion, recent investigations with optical research engines have explored the effects of the in-cylinder flows on spray formation in detail by using advanced optical diagnostics. In an early study, Serras-Pereira et al.¹⁰ recognized that the flow significantly affects spray morphology by comparing Mie scatter imaging of multi-hole injection sprays in ambient chamber conditions with part-load engine sprays. Marchi et al.¹¹ observed a reduction in the angle of a hollow-cone spray due to the flow induced by a first injection and Stiehl et al.¹² observed a similar trend in that with more than one hollow-cone injection, subsequent injections exhibited more cycle-to-cycle variations (CCVs) and an upward flow toward the cylinder head was identified as the main contributor to the spray deformation. In a subsequent study by Stiehl et al.¹³

simultaneous particle image velocimetry (PIV) and Mie scatter imaging revealed correlations between the tumble motion and the spray formation of a second hollow-cone spray, while the first spray remained largely undisturbed. The addition of a hollow-cone spray into a motored engine flow was shown by Peterson et al.¹⁴ to increase the turbulent kinetic energy, shear, and vorticity distributions by means of comparing tomographic PIV from experiments with and without spray. In a more recent investigation, Chen et al.¹⁵ used PIV to focus on the effects of a multi-hole injector spray on the ensuing flow field in early and late injection and found that the sprays did not significantly increase CCVs of the air flow, especially by the time of ignition. Finally, Sharma et al.¹⁶ compared the spray droplet size and velocity from a multi-hole injector in a constant volume chamber (CVC) and in a fired engine environment and found that the in-cylinder flows significantly hindered the spray droplet velocities. While the aforementioned investigations have widely advanced the field of DISI engine research, many of the findings are injector specific and none of them examined in detail and quantified the effects of the in-cylinder flow on macroscopic spray morphology for early injection.

In the pursuit of pooling the knowledge and resources of multiple research institutions around the world into the better understanding of the topic of spray-guided DISI combustion, the Engine Combustion Network (ECN) established a standardized multi-hole injector geometry with certain operating guidelines as a common framework for collaborative studies. The ECN's¹⁷ gasoline operating conditions, the so-called *Spray G* conditions have expanded from the high-density late injection standard *Spray G*, to a low-density early injection flash boiling *Spray G2* condition, to an ambient density early injection *Spray G3* condition, and to four other conditions over a wide range of parameters which are supposed to cover most of the possible phenomena involved in multi-hole spray-guided engine combustion. The injector used for this collaborative effort has eight evenly spaced holes, each with an orifice drill angle of 37°. A wide range of research has been conducted to study the injector and the *Spray G* operating conditions (OCs) using advanced imaging techniques in CVC experiments through spray morphology and injector detail characterization¹⁸⁻²¹ and multi-parameter inter-plume aerodynamics measurements.²²

Recent experiments have combined the *Spray G* injector and operating conditions in more realistic configurations by using optical research engines, instead of CVCs, for a more complex injection environment including in-cylinder motion. First, through Mie scatter imaging in the bottom view of an optical research engine, it was shown that engine speed plays a large role in the spray characteristics of early injection *Spray G2* and *G3*, indicating that CVC experiments can miss important phenomena involved in the spray-flow interaction.²³ Then expanding upon these findings, a joint

Table 1. Darmstadt engine and ECN Spray G2 and G3 injection parameters.

Parameter	Engine			
Cylinder head configuration	Spray-guided 4V pent-roof			
Spray G injector number	AV67-027			
Injector angle (°)	8			
Bore × stroke (mm)	86 × 86			
Compression ratio (–)	8.7			

Parameter	Engine spray G2	ECN spray G2 ¹⁷	Engine spray G3	ECN spray G3 ¹⁷
Facility	Darmstadt	ECN CVC	Darmstadt	ECN CVC
Fuel	Iso-octane	Iso-octane	Iso-octane	Iso-octane
Bulk gas	Air (dry)	0% O ₂	Air (dry)	0% O ₂
Engine speed (rpm)	800/1500	–	800/1500	–
Electronic SOI (°CA)	–270	–	–270	–
Hydraulic SOI (°CA)	–268.56/–267.29	–	–268.56/–267.29	–
Elec. inj. Duration (ms)	0.680 (Mie)/0.660 (PIV)	0.680	0.680 (Mie)/0.660 (PIV)	0.680
Hydr. inj. duration (ms)	0.780 (Mie)/0.760 (PIV)	0.780	0.780 (Mie)/0.760 (PIV)	0.780
Gas pressure at hydr. SOI (bar)	0.4	0.5	0.95	1.0
Gas density at hydr. SOI (kg/m ³)	0.45	0.5	1.08	1.12
Fuel pressure (bar)	200	200	200	200
Fuel temperature (°C)	60	90	60	90
Fuel mass (mg/cycle)	10 (estimated)	10	10 (estimated)	10

effort between two optical research engine groups equipped with Spray G injectors was carried out by studying the in-cylinder flows by means of PIV and their effects on spray morphology in late injection.²⁴ The results of the late injection investigations have shown that higher engine speeds lead to a more stable spray (angle) since the upward velocity induced by the piston in compression acts against the downward spray plumes and helps limit interactions between individual plumes.²⁴

With the availability of experimental data sets from different research institutions, numerical models have been developed to simulate Spray G, first in the CVC environment,^{25,26} then in the motored engine environment,²⁷ using open source code based on Reynolds-averaged Navier–Stokes (RANS). While these studies show promising progress in the field of high fidelity spray modeling, more experimental data are required to help identify the complex relationships involved in DISI engine operation and to equip researchers with accurate validation data in these environments.

Previous experimental investigations have shown that the in-cylinder velocity plays a crucial role in the development of sprays, but few investigations have quantified the effects of the flow on the spray morphology. With the goal of increasing the experimental database and decreasing the knowledge gap of Spray G DISI engine operation, this work uses advanced laser diagnostics and imaging techniques to provide a comprehensive study of early injection Spray G in increasingly complex research engine experiments by examining the effects of bulk gas density and in-cylinder flows on the spray development. This work is organized as follows: first, the engine test stand as well as diagnostic and post-processing methodologies are introduced. Then, the in-cylinder velocity and its

implications on spray atomization are examined. Afterward, the effects of decreasing bulk gas density and increasing in-cylinder velocity on spray shape evolution and inter-plume interaction are investigated. The results and discussion are then completed with a comparison of the morphology of each OC as well as a simplified no-flow engine spray case, which directly exemplifies the strong influence of in-cylinder flows on direct injection sprays. Finally, conclusions about early injection Spray G in DISI configurations are discussed and recommendations for future research topics are made.

Experimental setup

Engine test bench

Measurements were conducted at the Technical University of Darmstadt in a well-documented, well-characterized optical research engine test bench (*Darmstadt engine*).^{28–30} The single-cylinder spark-ignition research engine from AVL consists of a Bowditch piston extension, flat quartz glass piston surface, and a quartz glass cylinder liner for optical access. A four-valve spray-guided cylinder head configuration was employed, in which the Spray G injector and spark plug were both nearly vertically mounted and visible through the pent-roof quartz glass access. Table 1 shows the most relevant parameters for the Darmstadt engine configuration and Spray G injector used in this study. The early injection Spray G conditions outlined by the ECN¹⁷ use CVCs for precisely controlled characterization measurements.^{19,20} The engine experiments were conducted using the four principle operating conditions (OCs) of the Darmstadt engine using two intake pressures and two engine speeds, as shown in Table 2.

Table 2. Standard operating conditions of the Darmstadt engine.

Engine speed	Intake pressure	
	0.95 bar	0.4 bar
800 rpm	A	B
1500 rpm	C	D

Since the fuel temperature in this experiment was tied to the standard coolant temperature of 60°C, flash boiling was not achieved for cases B and D. Nevertheless, the OCs of early injection Spray G with the parameters of Table 1 are closely related to the Spray G2 (*Flash Boiling*) and G3 (*Early Injection*) condition outlined by the ECN.¹⁷ Fuel temperature aside, one more difference between the measurements and the ECN's conditions is in the bulk gas density, as the in-cylinder gas temperature depends on the cylinder head's temperature equilibrium. The in-cylinder temperature was estimated using the intake temperature as well as in-cylinder gas temperature measurements.³¹ Using such an estimation, the air density for case A and C at hydraulic start of injection (SOI) was 1.08 kg/m³, while that of Spray G3 is 1.12 kg/m³, a difference of 4.7 %. Furthermore, the bulk air density for OCs B and D was 0.45 kg/m³, while Spray G2 is 0.5 kg/m³, a difference of 10.1 %. The densities of the spray conditions within the engine and ECN guidelines are shown in Table 1 for comparison. Additional information regarding the Darmstadt engine test bench can be found in Baum et al.²⁸ and Freudenhammer et al.²⁹

Optical arrangement

Four experimental campaigns were conducted in this work to provide a comprehensive study of early injection Spray G in an optical engine environment. The optical setups of PIV and Mie scatter imaging are described in the following sections and a summary of the experimental details is found in Table 3. In addition, a schematic detailing the engine geometry and different optical setups is provided in Figure 1.

Particle image velocimetry. In-cylinder flow was measured using high-speed PIV by illuminating silicon oil droplets ($\approx 0.5 \mu\text{m}$, DOWSIL 510, Dow Corning) with two laser sheets (532 nm, 1.3 mm thickness at 13.5 % of the maximum intensity) introduced by frequency-doubled Nd:YAG cavities through the optical piston via the Bowditch extension and piston mirror. Flow data used in this work comes from two different experimental campaigns, designated Experiment I and Experiment II, as outlined in Table 3.

For Experiment I, the main focus of this study, a Phantom v711 high-speed CMOS camera equipped with a Sigma lens ($f = 105 \text{ mm}$, $f/11$, 20 extension

Table 3. Summary of experimental setups.

Parameter	Experiment I	Experiment II	Experiment III	Experiment IV
Description	HS PIV – spray	HS PIV – motored	Mie scat. – motored	Mie scat. – NF
Light source	Nd:YAG sheet (532 nm)	Nd:YAG sheet (532 nm)	LED volume (525 nm)	Nd:YVO ₄ volume (532 nm)
Optics	–50 mm cyl. + –200 mm cyl. + 1000 mm cyl.	–50 mm cyl. + –200 mm cyl. + 1000 mm cyl.	Aspheric condenser lens 40 mm	–50 mm cyl. + 1000 mm cyl. + 200 mm cyl. + –50 mm cyl.
Camera	Phantom v711	Photron Fastcam SA-X2	Phantom v711	Phantom UHS v2640
Lens	Sigma $f = 105 \text{ mm} + f/11 + 20 \text{ mm extension}$	Sigma $f = 105 \text{ mm} + f/11 + 20 \text{ mm extension}$	Nikon $f = 50 \text{ mm} + f/5.6$	Nikon $f = 85 \text{ mm} + f/16 + 35 \text{ mm extension}$
Rep. rate (Hz)	4800 at 800 rpm + 4500 at 1500 rpm	960 at 800 rpm + 1800 at 1500 rpm	16,000	25,000
Int. window or pixel size	(2.54 mm) ² int. window + 635 μm vector spacing	(2.02 mm) ² int. window + 504 μm vector spacing	130 $\mu\text{m}/\text{pixel}$	65.2 $\mu\text{m}/\text{pixel}$

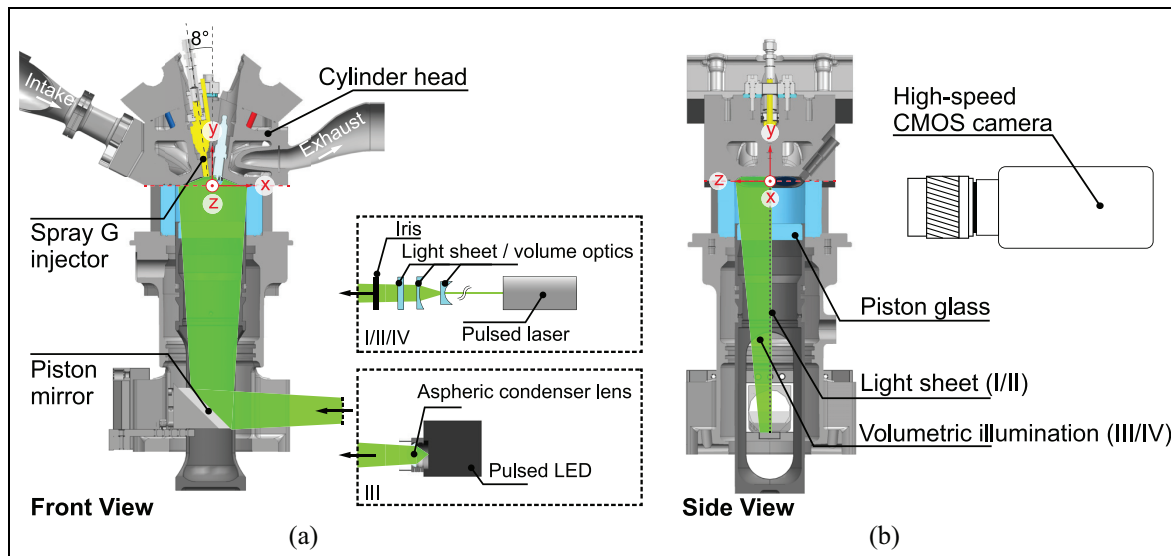


Figure 1. Experimental setups used within this study. (a) Section view of the x - y plane including the optical arrangement of the employed illumination sources. The injector and spark plug are located centrally in the x - y plane as indicated by the section view. (b) Section view of the y - z plane.

tube) was used to acquire image pairs from the side of the glass cylinder, maximizing the possible field-of-view of the combustion chamber ($58 \times 63 \text{ mm}^2$). Image pairs were acquired at a crank angle (CA) resolution of 1° CA for an engine speed of 800 rpm (4.8 kHz) and 2° CA for an engine speed of 1500 rpm (4.5 kHz) with varying time separation between laser pulses dt from $51 \mu\text{s}$ to as low as $3 \mu\text{s}$.

Experiment II is used in this work simply to provide context for the in-cylinder flows without the direct injection of fuel and represents the well-documented PIV approach of Welch et al.³² For details on Experiment II not found in Table 3 and the processing of image pairs, please refer to Welch et al.³²

Mie scatter imaging. Experiment III represents the high-speed imaging of liquid spray using Mie scattering. Even though diffuse back-illumination (DBI) is the ECN's technique of choice for morphological comparisons, the authors of this work have chosen to use bottom illumination Mie scattering instead of DBI because of two reasons: firstly, the cylinder roof obstructs much of the incoming LED light from the diffuser, blocking about half of the spray from being illuminated; and secondly, the disadvantage of increased beam steering and the susceptibility of overestimation of the liquid phase of the spray associated with DBI.^{24,33} As shown in Figure 1, light from a pulsed LED equipped with an aspheric condenser lens was introduced to the cylinder volume via the piston mirror assembly and images were acquired from the side of the cylinder. The high-speed CMOS camera used for image acquisition was a Phantom v711 equipped with a Nikon lens ($f = 50 \text{ mm}$, $f/5.6$) operating at a frame-rate of 16 kHz.

In addition to the Mie scattering experiments described above, an additional no-flow (NF) experiment, Experiment IV, was conducted to act as a baseline for comparison. In the NF case, the engine's piston was completely replaced by an exit flow duct with a quartz glass bottom plate and the stationary intake valves were set to 9.21 mm, which corresponds with the valve lift at -270°CA , (270°CA before compression top dead center), allowing for an unobstructed open channel for the spray to travel through. The simplified open-engine geometry is introduced in Haussmann et al.³⁴ as a flow bench experiment; however, in this current study, no intake flow is introduced into the channel, the Spray G injector replaces a blank dummy injector, and sprays occur after a sufficient amount of time to allow residual fuel from previous sprays to evaporate and exit the channel (a purge of 0.517 kg/h was used to facilitate movement of residual gas). A mirror below the channel still allowed for bottom illumination from a volumetric light source of two Nd:YVO₄ high-speed laser cavities for a combined effective repetition rate of 25 kHz. No-flow Mie scatter images were acquired using a Phantom UHS v2640 high-speed CMOS camera equipped with a Nikon lens ($f = 85 \text{ mm}$, $f/16$, 35 mm extension tube) from the side of the engine cylinder in the same manner as the motored engine Mie scattering experiments.

Post-processing

Vector calculation. In both Experiment I and II data were pre-processed and vectors were calculated using the commercial software *DaVis 8.4*. A progression of five steps were followed to bring raw image pairs to processed vector fields:

1. *Image pre-processing* A spatial sliding background correction of pixel length 8 was used to reduce noise and reflections. In addition, a particle intensity normalization filter of length was applied to help increase particle contrast.
2. *Image masking* First a geometric mask followed by an algorithmic mask was applied to each image to remove areas of high multiple scattering due to highly reflective objects such as the spark plug, or in the case of Experiment I, the liquid spray. The algorithmic mask consisted of first a local standard deviation filter over 10 pixel, then with the new image, a minimum and maximum threshold of 9 and 350, respectively to remove the remaining stationary and non-illuminated objects from further calculation.
3. *Image correction* Before vector calculations began, the masked images had to be dewarped and scaled using a third order polynomial based on images acquired of a 3D calibration plate (LaVision plate 058-5).
4. *Vector calculation* Vectors were calculated using a cross-correlation PIV algorithm with multiple passes of decreasing window size. The first two passes used interrogation window (IW) sizes of 64×64 with 50% overlap. The final two passes decreased their window size to 32×32 with 75% overlap and employed the adaptive PIV Gaussian weighting function.
5. *Vector post-processing* Post-processing of vectors was executed without any smoothing. First a peak ratio criterion was applied which deletes any vectors whose first and second correlation peaks in the IW are below 1.3. Next, a universal outlier detection was applied, consisting of normalized median filter sliding in a 7×7 vector window. Finally, with the overlap of 75% a remove group criterion of five vectors was used, that is if less than five vectors out of the possible 16 are available, the entire group is removed. This is done to remove more spurious vectors that were missed by the median filter due to, for example, high reflections.

Vector files for each crank angle and cycle were then imported into *MATLAB* and the phase-average, that is, the average vector field at each crank angle over all cycles, was computed with a minimum of 25 vectors per IW required.

Regarding vector calculation and statistical uncertainties, possible sources of error have been extensively discussed for a similar PIV setup in the Darmstadt engine.³⁴ For the present work, phase-averaged uncertainties for Experiment I and II were estimated using the built-in correlation statistics approach included in *DaVis*.³⁵ The uncertainties range between $\approx 2\%$ and 4% within the relevant region of interest defined in Figure 3.

Spray boundary calculation. The detection of spray boundaries of Mie scatter images was conducted with in-house

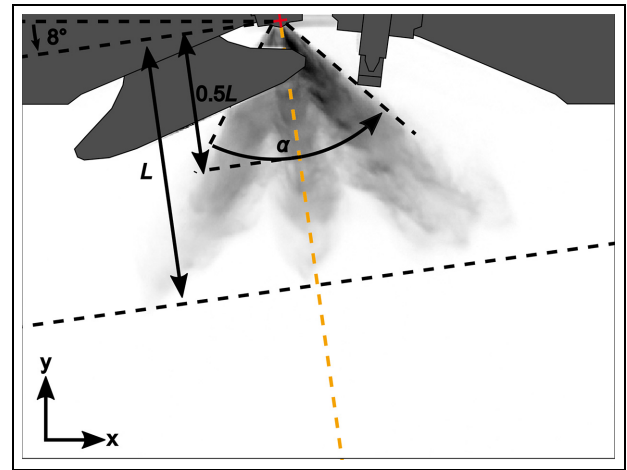


Figure 2. Definitions of geometrical parameters penetration length L and spray angle α .

MATLAB code and followed the same exact procedure as in Geschwindner et al.²⁴ and is summarized in four steps:

1. *Image correction* As with raw PIV images, the raw Mie scatter images were first dewarped and transformed into lab coordinates using the same 3D target and a third order polynomial.
2. *Image masking* In a similar manner to PIV image pre-processing objects such as the spark plug and intake valves were masked out to remove reflective engine features.
3. *Background subtraction and noise reduction* The mean of the first three images before injection was used as a background subtraction for all subsequent spray images and a 3×3 median filter was applied to reduce noise.
4. *Threshold definition and binarization* Each spray cycle was assigned a single threshold of the normalized intensity of the cycle. To define the threshold, the maximum intensity of the mean background image (which was previously subtracted) was added to the 2D spatial standard deviation of the mean background multiplied by a separation factor of 250. The separation factor of 250 was selected to create sufficient separation between the foreground and background signal and corresponds to the spatial placement of the segmentation edge in the region of the sharp intensity gradient at the spray's boundary. However, strong variations of the separation factor do not cause significant deviations in the calculated geometrical spray parameters.

Due to the slightly in-homogeneous intensities from the two laser cavities used in Experiment IV, a separate threshold was calculated for all images of each cavity, that is, two thresholds were calculated, one for odd-numbered images and one for even-numbered images. This resulted in a significantly different threshold value

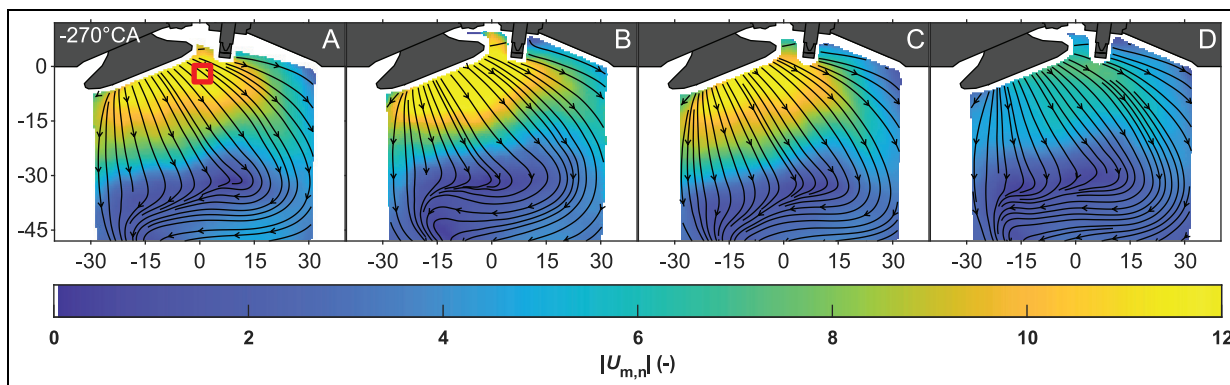


Figure 3. Phase-averaged flow fields of the velocity magnitude at -270°CA normalized by the piston speed. The red box in the first panel represents the region of interest for the velocity profile in Figure 4.

than the combined set of images. Yet, using two separate sets, the thresholds were very close (within a 10th of a percentage difference) and were therefore averaged to one single value. The resulting average threshold over all cycles for Experiment IV is 11.14 % while for Experiment III the values ranged from 5.33 % to 6.63 % of their maximum normalized intensity of each injection, depending on the OC.

Extraction of spray parameters. The axial penetration length L and spray angle α are geometric parameters calculated based on the binarized spray images using in-house *MATLAB* code. The axial penetration is defined as the maximum distance of the spray boundary from the injector tip along the injector axis. In accordance with the definition of Payri et al.,¹⁹ α is the angle between the lines determined by a linear least-squares fit of the two outer edges of the spray boundary between 1 % and 50 % of the maximum L . Figure 2 provides a visual representation of the defined parameters.

Results and discussion

In-cylinder velocity

Velocity without injection. Before investigating the effects of the flow field on the evolution of sprays, it is first important to understand and characterize the in-cylinder flows before SOI. Under the four standard operating conditions (OCs) of the Darmstadt engine, shown in Table 2, phase-averaged flow fields of the velocity magnitude at -270°CA normalized by the piston speed in the symmetry plane $|U_{m,n}|$ are shown in Figure 3. The phase-averaged flow fields represent the average of 222 cycles for OC A and B and 296 cycles for C and D at -270°CA , with the blue-yellow color-map indicating the velocity magnitude and the streamlines indicating the flow directions. Since the electronic injection signal for the early injection begins at -270°CA , these flow fields reflect the state of the in-cylinder motion just before the spray commences.

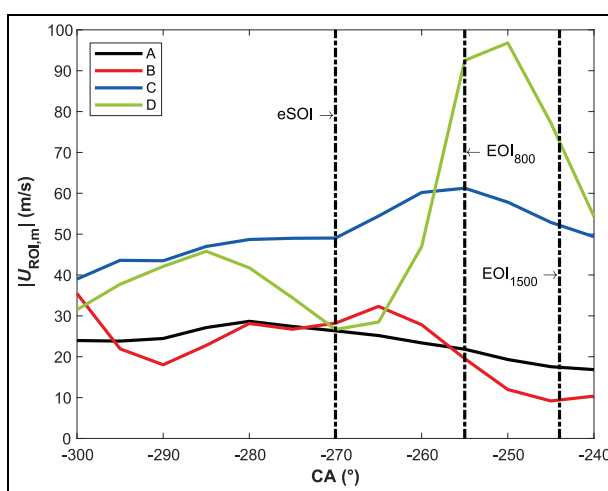


Figure 4. Phase-averaged velocity profiles near the intake valve without injection. The time range shown represents the duration of an injection event. The velocities are obtained from the average of the region of interest shown in the first panel of Figure 3. The vertical dashed lines represent the electronic start of injection and the end of injection for 800 and 1500 rpm.

In a previous study by Welch et al.,³² it has been shown that OCs B and D (part-load OCs) exhibit a pressure equalizing backflow from the cylinder to the intake pipe, due to the intake pressure being below atmospheric pressure. This induces pressure oscillations in the intake manifold, which ultimately affect the intake flow. As shown in Figure 3, OC D has much lower normalized velocities than OC B at the time of electronic start of injection (eSOI), despite all OCs having similar flow structures (indicated by the streamlines).

Due to the transient local pressure ratio at the valves in the case of part-load operation, the equalization of the pressure induces strong fluctuations in the flows entering the cylinder. Figure 4 shows the effects of the pressure instabilities on the average absolute intake velocity magnitude in the region of interest below the injector, highlighted by the red box in the flow field of

OC A in Figure 3. Figure 4 also highlights the definition of a “theoretical spray event” by showing the timing for eSOI and the end of injection (EOI) for the two engine speeds. The timing for EOI is determined from Experiment II (PIV with spray), by the absence of strong Mie scattering stemming from dense liquid spray clouds and large droplets in the laser sheet, which induce a bias in the vector calculations as well as more deleted vectors (further visualization of the 2D-projected area obtained on a planar slice at EOI is provided by Figure 7; in the case of Figure 4 no fuel is injected). The intake velocity profiles during theoretical injection show that the intake flow of OCs A and B slightly decelerates during a theoretical injection event, yet these flows may still be considered relatively stable. Operating condition C also exhibits a relatively stable intake flow as it first accelerates then steadies out before decelerating to similar speeds as before the theoretical injection event. On the other hand, in the case of OC D, which has a liquid injection duration spanning from -267.3°CA to -261.4°CA , the flow rapidly accelerates to velocities far exceeding those of OCs A and B and therefore, introduces a high amount of turbulence into the cylinder by the end of the injection. While these absolute velocity magnitude comparisons actually reflect the in-cylinder intake flows without injection occurring, it is safe to assume that the flows follow the same trends when a spray is injected; this will be further explored in the next section. It is important to point out again, that these velocities only reflect one region of interest below the injector; yet, the influx of flow in this region is still representative of the bulk intake flow, which has also been demonstrated by flow measurements in the valve plane.³²

Turbulent kinetic energy and mixing. In the quiescent environment of a constant volume chamber, evaporation of a multi-hole injector spray is achieved through a coupling of the effects of the surrounding gas density, temperature, and the turbulence generated by the spray itself, which is designed to be significant. Yet, the actual application for such injectors includes the complex addition of turbulent flows and moving engine parts, constantly changing the boundary conditions (chamber pressure and temperature) as the piston and valves move. The ECN gasoline injector OCs considered in this work represent a short, early injection at ambient (G3, here case A and C) and part-load (G2 flash boiling, here case B and D) pressures. Global pressure and temperature are constant in the case of early injection, which reduces the complexity of such a problem, minimizing the consequential phenomena to the chosen intake load and the in-cylinder flows. The parametric variations of engine speeds and intake pressures of OCs A through D allow the examination of the effects of these properties on the evolution, evaporation, and mixing of sprays within a dynamic, highly turbulent in-cylinder flow field. The turbulent kinetic energy k ,

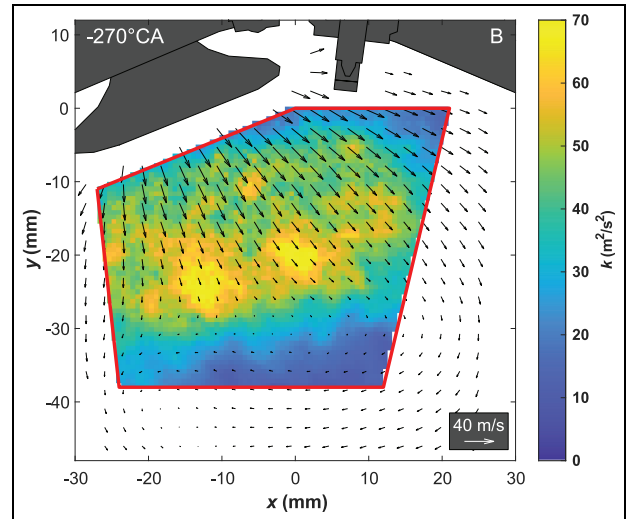


Figure 5. Global turbulent kinetic energy k at -270°CA for OC B (800 rpm, 0.4 bar) within a conservative mask (red line). The blue-yellow colormap represents k and the black arrows represent the phase-averaged velocity magnitude (arrow length relative to the legend in the bottom right corner) and direction.

defined as the mean kinetic energy per unit mass in the fluctuating velocity field,³⁶ can be used to examine the evolution of turbulence in a flow field through the change of measured root mean square velocity fluctuations. In terms of the two-dimensional $x - y$ velocity components u and v typical of experimental data, two-dimensional k can be written as:

$$k = \frac{1}{2} \left(\overline{(u')^2} + \overline{(v')^2} \right) \quad (1)$$

or simply:

$$k = \frac{1}{2} (S_x^2 + S_y^2) \quad (2)$$

where the over-line bar and “prime” in equation (1) denote the mean and fluctuations from the mean, respectively, and S in equation (2) denotes the standard deviation of the planar velocity components. Turbulent kinetic energy over time provides context for the state of the in-cylinder gas motion before an injection event and allows the determination of the amount of turbulence introduced into the system by the spray motion. Figure 5 shows an example k field within a mask marked by the red outline as well as the phase-averaged velocity indicated by the black arrows of scaled length and direction for OC B at -270°CA . For the following analysis of k , the mean k within the same mask shown in Figure 5 is used for each OC and at each CAD to provide a global quantification of turbulence in the approximate cross-sectional area where the spray appears. Such a method for quantifying turbulence neglects the spatial distribution of local smaller-scale flow structures since the mask (relative to this engine’s optical access) is nearly global. However, the spatial mean k of this region of interest (where the liquid spray

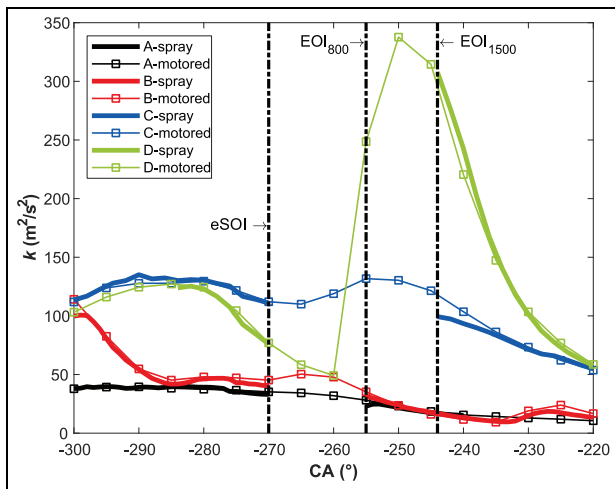


Figure 6. Mean turbulent kinetic energy k of the masked region shown in Figure 5 for OCs A through D from experiments with spray and without spray (motored) during intake. When vectors are affected by the presence of liquid spray, k is removed (indicated by black lines labeled EOI).

occurs) does capture the effects of all of the resolved scales of this technique and can be compared over time and over different OCs. As shown in Figure 5, the greatest k magnitude distribution just before the liquid spray begins is spread in a crescent shape 20–40 from the intake valves. This phenomenon can be explained by the increase in velocity fluctuations just beyond the high-velocity intake flow region of the symmetry plane. The spots of higher k are representative of the high gradient of the ensemble average velocity visible, for example, in the orange flow region for OC B in Figure 3.

The turbulent kinetic energy k for OCs A through D with spray and without spray (labeled as *motored*) during intake is shown in Figure 6. Once again, for this visualization, EOI is defined as the end of the effect of the liquid spray on the PIV calculations and k is removed from the plot from SOI until EOI because of the absence of a sufficient number of viable vectors. The overall shapes of the curves reflect the intake velocity profile taken from the red region of interest shown in Figure 3, which indicates a correlation between mean intake velocity magnitude and velocity component fluctuations. When comparing experiments with and without injections, Figure 6 reveals that there is not a significant increase in k due to the highly turbulent spray. Shortly after the indicated EOI for the higher engine speed cases, the remaining fuel in the region of interest should be sufficiently evaporated so that the droplets do not affect the calculations through excess Mie scattering in the laser sheet. However, in the case of C, it appears that the remaining fuel droplets have an influence on the vector calculations, creating a bias because the large scattered fuel droplets cannot follow the flow as well as the oil seeding droplets. At -234°CA , k in the spray case of C begins to converge with that of the motored case, indicating a more

accurate end of the effect of the spray on the flow field measurement, that is, a better EOI. The amount of turbulence, or better, lack thereof, added to the cylinder by the spray may stem from a number of factors such as the time of injection, injection duration, engine speed, intake pressure, and injection pressure. However, it seems likely in this case that the lack of increase in k comes mainly from the field of view of the PIV experiment and the chosen region of interest, which only consists of an area directly below of the injector tip. Much of the added turbulence is likely convected downwards with the motion of the bulk flow and adds to the formation of the tumble vortex, which is largely left out of the chosen region of interest until the middle of the compression stroke because the piston remains near bottom dead center within this time range.

While it is highly likely that k increases during the injection of a high-speed disperse phase, as observed in several previous studies,^{12,37,38} the strong multiple scattering of the fuel droplets render the flow fields at these times unusable for analysis. Yet, in a similar experiment by Chen et al.¹⁵ it was observed that in the case of early injection, the flow structures and k did not change at the time of ignition. During late compression when ignition occurs, the turbulence should already have broken down into smaller structures, which may not be well-captured with the spatial resolution and in the single plane of these measurements. This implies that while the flow may have a significant effect on the spray morphology during intake, the spray's effect on the flow is minimal, especially in late compression, when the turbulence is dissipated, a finding which aligns well with the conclusions drawn by Figure 6.

In the absence of evidence of an increase in turbulence due to the spray within the given region of interest, the interaction between the spray and in-cylinder velocity must be further analyzed. Perhaps the most important consideration in implementing a direct injection into an engine design is the evaporation and efficient mixing of the spray with the air. Without further optical techniques such as laser-induced fluorescence (LIF), it is difficult to quantify fuel-air mixing. However, using the Mie scattering of liquid fuel from a PIV experiment, it is possible to measure the relative evaporation of liquid fuel and assume that the fuel-air mixing is likely correlated with the rate of evaporation and in-cylinder velocity by summing the intensity of raw images and plotting the total intensity over time. Using such a method, the influence of seeding droplets and in-cylinder reflections on the intensity of the raw image must be eliminated before the sum of counts is performed so that the intensity only due to the presence of liquid fuel is considered. To achieve this strategy, first the average image over all cycles before (-270°CA) and after liquid injection is taken, resulting in an image with a uniform distribution of seed appearing blurred throughout the illuminated plane before injection and an average spray image (at each CAD) with the

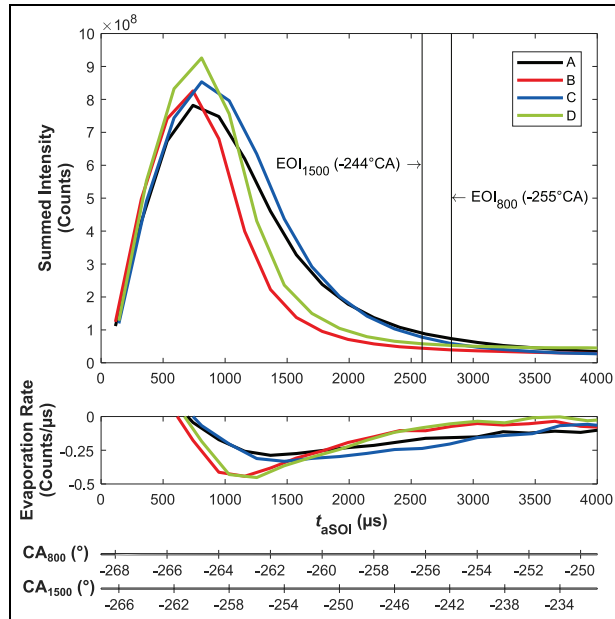


Figure 7. Estimation of the evaporation of the liquid spray after the start of injection. Top panel: sum of the spatial intensity by the CMOS camera. Bottom panel: rate of evaporation assumed to be the rate of change of the summed intensity at each time aSOI. The corresponding crank angles are provided for reference.

uniform blurred seed surrounding the spray. Then, a mask is applied to reflective objects such as the intake valves, spark plug, and cylinder roof for all images. Finally, the average image before spray is subtracted from the average spray images and the spatial intensity is summed, resulting in a time-series of spatial intensity.

The top panel of Figure 7 displays the evolution of the total intensity and the bottom panel shows the assumed rate of evaporation for each OC. Here, assumed rate of evaporation refers to the rate of change of the summed spatial intensity of each image over time and thus reveals a quantity which is assumed to be the evaporation rate. Once again, the real hydraulic injection duration is $780 \mu\text{s}$, which can be observed as the peak in summed intensity in the top panel, and EOI is chosen as points where the summed intensity is nearly zero. Two main conclusions may be drawn from this figure: first, the greater ambient gas density found in OCs A and C results in slower fuel evaporation from EOI until approximately $t_{aSOI} = 1500 \mu\text{s}$, at which point the intensity of B and D is quickly approaching zero counts. The rapid rate of evaporation for OC B and D is due to the lower exertion on the surface of the droplets at lower ambient gas pressures (with constant intake temperature). Second, with increasing in-cylinder velocity, the magnitude of the evaporation rate is generally higher (bottom panel) from $t_{aSOI} = 1000 \mu\text{s}$ to $t_{aSOI} = 2500 \mu\text{s}$. For this time window, the in-cylinder velocities for C and D reach a maximum as the valve lifts approach their maximums (at -250°CA), while for

A and B, the velocities are decreasing. When comparing cases with the same intake pressure, the differences of intake flow at this time period play their biggest roles in affecting the rate of evaporation. Increased rates of evaporation during this critical time window stem from the availability of fresh air for the spray to evaporate into, since fuel is more likely to evaporate when the local mixture is not saturated.

A tertiary conclusion from Figure 7 can be drawn from the relative magnitudes of the summed intensities in that with increasing total intensities, the cross-sectional liquid spray area appears to be larger. A larger spray area can manifest itself in several morphological features, for example, greater axial penetration or cross-sectional spray area. In the next section of this paper, the effects of variations of the in-cylinder pressure and velocity on the liquid spray shape will be examined in more detail.

Spray morphology

In this section, results from the volumetric Mie scatter imaging approach are used to further evaluate the effect of pressure and in-cylinder velocity on the spray evolution.

Plume interaction: Wall and inter-plume. One aspect of spray experiments in engine configurations that is largely negligible in pressure chamber experiments is the affect of wall wetting, that is, spray impingement on solid surfaces such as the piston. In ideal DISI engine designs, the injector and timing would be designed in a way to avoid such plume-wall interactions. Yet, this is a difficult task considering the relative length of spray duration required to achieve a combustible mixture compared with the positions of moving engine parts; in early injection cases the spray of a multi-hole injector might interact with the intake valves, spark plug, the piston surface (depending on engine speed and injection timing), and/or the cylinder walls. Therefore, it is important to acknowledge this phenomenon and understand its effects on spray and subsequent engine performance.

Figure 8 shows the spray evolution of instantaneous raw Mie scatter images for each OC (every 4th image displayed). The liquid spray, represented by illuminated liquid droplets, is displayed from the beginning, middle, and end of a typical spray event. Due to the line-of-sight used in this setup, individual plumes cannot be distinguished and the intake valves obstruct part of the view of the volumetric spray measurement. However, it appears that beginning from early spray at $198.7 \mu\text{s}$ aSOI that the outer plume on the exhaust side comes into contact with the spark plug for all cases. This phenomenon is even more clearly visible in the case of B and D at $698.7 \mu\text{s}$ aSOI, where white streaks due to wetting appear downstream of the spark plug. While

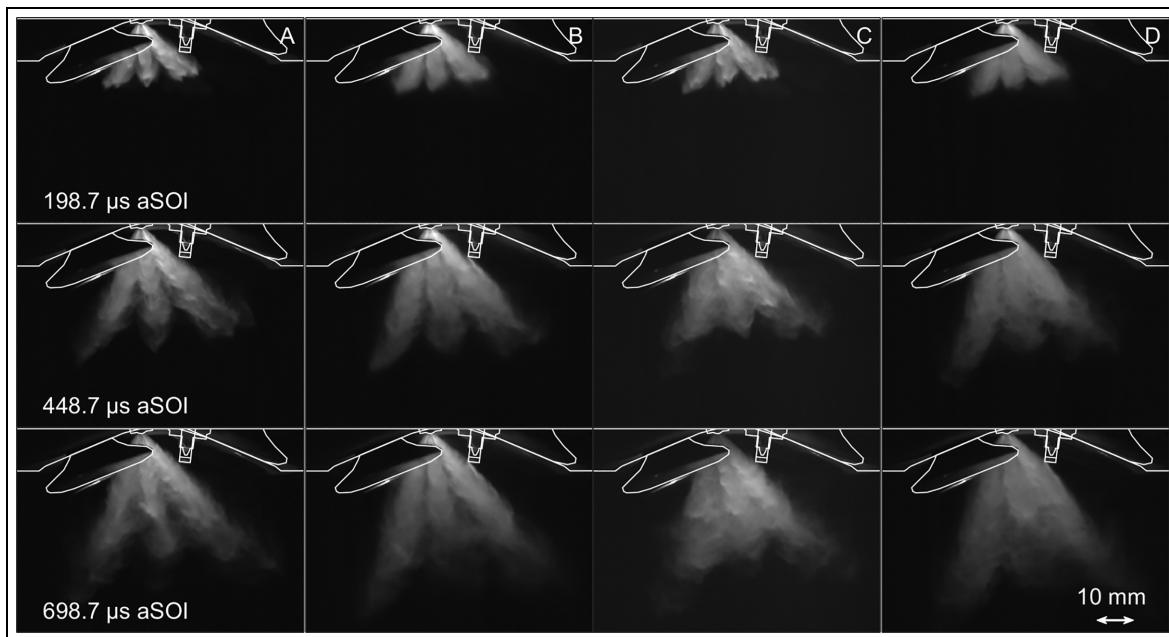


Figure 8. Evolution of instantaneous Mie scatter images for each OC.

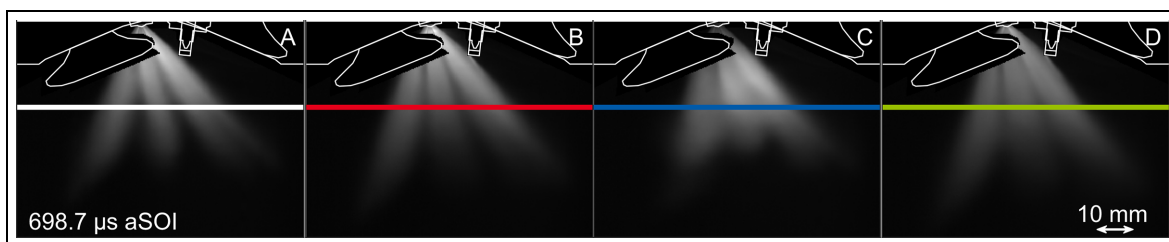


Figure 9. Average normalized Mie scatter image at $698.7 \mu\text{s aSOI}$. Color-coded lines represent the line profiles of Figure 10.

the effects of such wall wetting are difficult to quantify using the given experimental technique, it appears in the cases of B and D that this spray-wall interaction causes a deficiency in axial penetration on the exhaust-side plumes. The wall wetting observed in these images is supplemented by the findings of Pati et al.²⁷ in which the same engine using OC A with Spray G3 was simulated, and a fuel film was observed not only on the intake valves, but also on cylinder walls and even the piston surface, despite the early injection and short duration of Spray G3.

As previously stated, the line-of-sight of these volumetric Mie scattering measurements does not allow direct visualization of individual plumes and important quantities for spray characterization, such as the individual plume angle, are still missing. However, a measure of the amount of interaction between plumes can be deduced by examining the Mie scatter images. Figure 9 displays the normalized average spray of 100 cycles at $698.7 \mu\text{s aSOI}$. For this normalization, the

images were first averaged, then the images were normalized to the highest intensity out of the four cases for a valid comparison between OCs. But examining the average spray images also reveals the extent to which individual plumes can be distinguished. It is clear that OC C has the most plume-to-plume interaction since there are no clear lines separating them. This can also be observed at the same time-step in Figure 8; however, in the instantaneous snapshots, plumes in case D also appear to have merged in a similar manner to C.

To further quantify the inter-plume interaction, Figure 10 plots the normalized intensity profiles indicated by the colored lines in Figure 9. The vertical location of the line profiles was selected to be at approximately 50% of the penetration length, but the trends were found to hold true for other locations. Increasing the engine speed for the case of full-load intake pressures has the most obvious effect on plume-to-plume interaction as displayed in Figure 10 by the

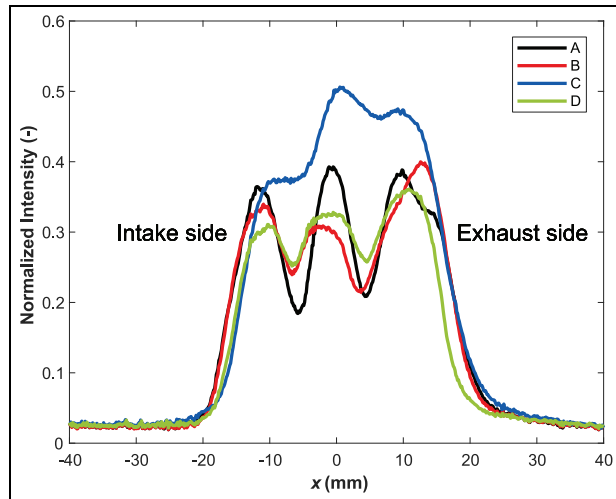


Figure 10. Normalized intensity profile along lines from Figure 9. Plume-to-plume interaction indicated by the distinction of plumes from one another.

lack of distinct peaks of intensity for C. The effects of intake pressure are also evident by the large difference between peaks and troughs of the profile for A compared with B.

In addition to plume-to-plume interaction, Figure 10 can also convey a comparison between the cases for the global spray angle as well as the tendency of the spray to evolve in a certain direction. Since the spray angle calculated from binarized Mie scatter images will be described in more detail in the following section, it will only be pointed out that D appears to have the smallest opening angle, indicated by the comparatively narrow intensity profile. While D has an intensity profile much narrower than the other cases, case C appears to have a skewed profile toward the exhaust side (right side of Figure 10). This is interesting because it indicates that the strong intake flow, which is characterized in Figure 3 as a distinctly downward and rightward (piston- and exhaust valve-directed) flow with high magnitudes (Figure 4) near the spray region, not only affects the evaporation and inter-plume interaction, but it also seems to push the bulk spray shape in the direction of the exhaust valves. If OC A and B are considered nearly symmetric, it appears that C has significant asymmetry in its intensity profile.

Sphicas et al.²² studied the inter-plume interaction and its effect on the flow recirculation in the spray center in a constant volume chamber. It was hypothesized that the spray angle is stabilized by radial air entrainment. Intense inter-plume interaction stops this radial entrainment and can ultimately lead to a collapse of the spray toward the center. Chen et al.¹⁵ found a weakening of the engine intake flow inside the spray along the injector axis, which can be attributed to a superimposed recirculation induced by the spray. In the current work, the spray orientation and multi-scattering effects restrict the amount of flow information that could be gathered in the spray center. Still,

when comparing flow fields at the spray tip along the injector axis, the downward-directed intake flow does not seem to weaken (not shown), which limits such a phenomena to the inaccessible region inside the spray.

In this context, compared to quiescent conditions, the intake flow could have three effects on the spray: first, a stronger intake flow reduces the slip velocity between spray and air, and therefore reduces air entrainment. This possible difference in air entrainment in the engine case weakens the importance of radial air flow stabilizing the spray center and ultimately spray angle. In Figures 9 and 10 this effect is supported by the presence of strong inter-plume interactions in case C and D, but total or extreme collapse never occurs. Second, with increasing intake velocity, the drag reorients the plumes toward the flow direction, which leads to asymmetric spray evolution and smaller spray angles. Third, the intake flow induces quicker evaporation due to higher dispersion and turbulent mixing.

In both cases of higher engine speed, turbulence, and its accompanying phenomena, namely enhanced dispersion of liquid droplets and mixing, as well as the directed intake flow, cause a noticeable difference in the spray angle and inter-plume interaction when compared with the lower engine speed cases. These effects will be further explored in the following section.

Binarized spray evolution. Using the binarization technique outlined in the experimental setup and by Geschwindner et al.,²⁴ the spray morphology is further examined and quantities are derived for further characterization and comparison. A useful visualization for the comparison of spray morphology is a probability map, in which the phase-average of all binarized spray images is plotted to show the statistical likelihood that liquid spray will occur in a position. The evolution of the binarized probability for all cases is displayed in Figure 11. The blue-yellow colormap makes it clear that cycle-to-cycle variations (CCVs) are quite insignificant on the onset of spray by the almost completely yellow spray probability (meaning 100% probability) in each case. Yet, CCVs also appear to remain small throughout the entire spray event, indicating a stable, repeatable injection at each condition. However, as is common throughout this work, the different OCs vary greatly from one another, a fact that highlights the importance of such parametric studies in gaining a more complete understanding of the multi-hole injection in engine operation, since the engine speed and load of an engine is constantly changing in normal operation. Interestingly, case B and D appear to have a very similar liquid spray morphology evolution despite the different levels of turbulence, especially at EOI. Yet, upon the closer inspection of spray morphology quantities, more differences emerge.

It is clear that variations in flow properties from the different OCs cause morphological changes in the spray. From Figure 11 it is possible to observe a trend

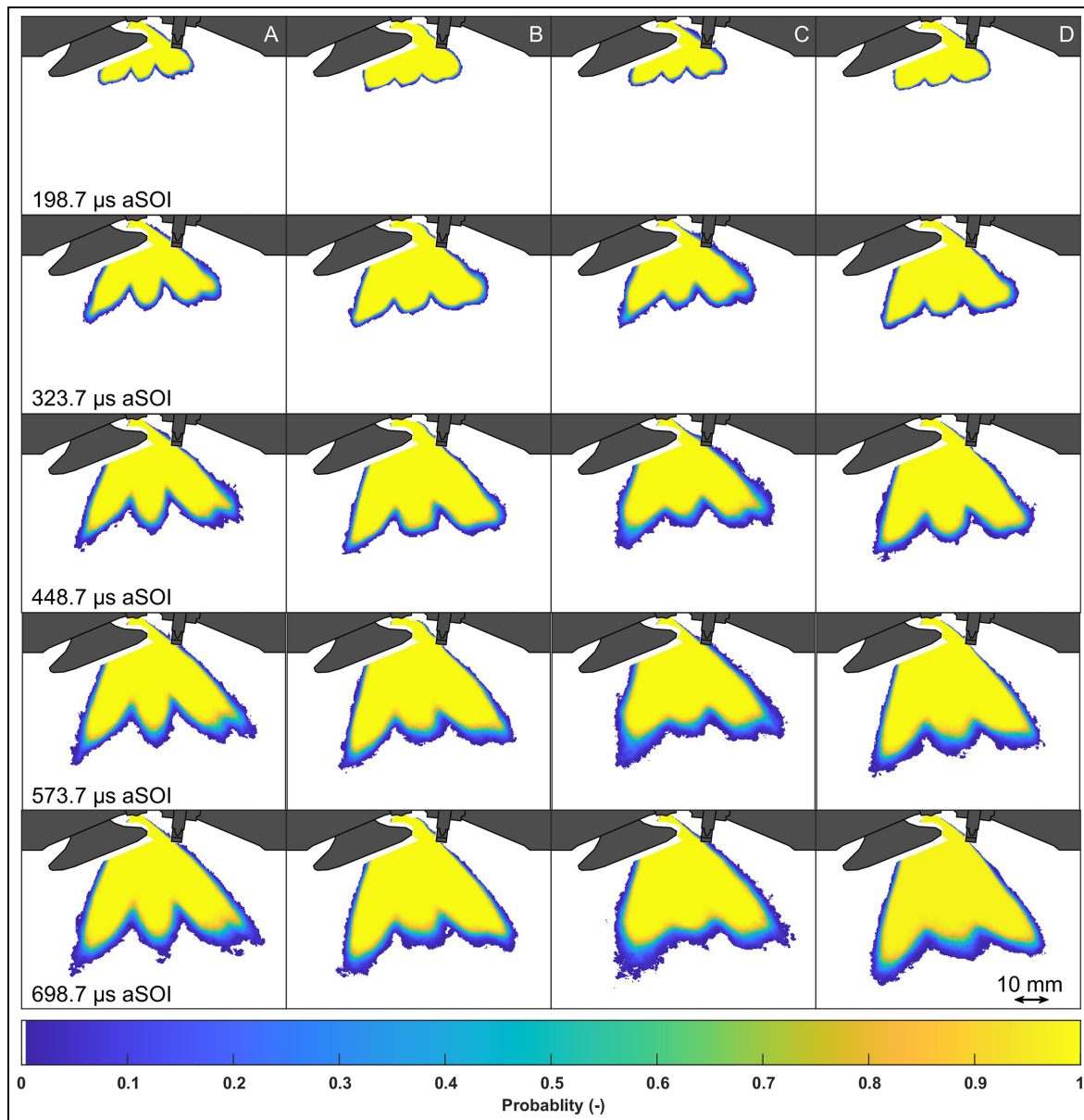


Figure 11. Evolution of binarized spray probability obtained from volumetric Mie scattering (Experiment III).

of decreasing liquid spray symmetry with increasing in-cylinder velocity, as OC A appears to have a more symmetric distribution about the spray axis than OC C. By introducing Experiment IV into the comparison, the engine spray without flow, this trend confirmed. Figure 12 displays the average liquid spray and its calculated boundary for the NF case at $680 \mu\text{s aSOI}$ as well as the outlines of the average liquid spray boundary for the two nearly atmospheric OCs A and C at $698.7 \mu\text{s aSOI}$. Although Experiments III and IV employ slightly different illumination techniques and have different camera systems, the principles of volumetric Mie scattering apply to both data sets and make this a valuable comparison. A number of observations can be made through this comparison, the first being that the penetration length of the NF case is far greater than the motored cases. This can be attributed to the lack of

turbulent dispersion as well as less evaporation in the absence of intake flow interacting with the spray. In addition, the spray opening angle decreases significantly with the presence of flow and decreases further with higher speeds. Not only does this tendency of increasing spray collapse with increasing intake flow velocity emerge, but also the boundaries on either side of sprays reveal that on the exhaust side, with or without flow, the liquid spray expands on a similar trajectory. A slight variation from this tendency is that the NF case tapers down at the plume tip, which probably occurs because of the limited illumination region. Conversely, on the intake side, increasing flow velocity brings an angle shift toward the exhaust, which is visible by the intake-side and middle plumes, while the NF case seems to exhibit a spray expanding symmetrically along the spray axis. One final observation is that in

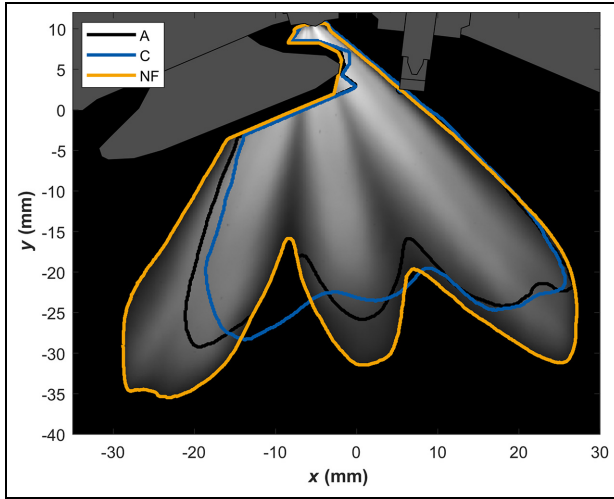


Figure 12. Average spray in a no-flow (NF) configuration in which the piston is removed. The average binarized spray contour is displayed for the near-atmospheric operating conditions.

Table 4. Sample standard deviations for L and α at the middle ($t_{mid} \approx 320 \mu\text{s}$ aSOI) and end ($t_{end} \approx 640 \mu\text{s}$ aSOI) of liquid injection.

OC	L_{mid} (mm)	L_{end} (mm)	α_{mid} ($^\circ$)	α_{end} ($^\circ$)
A	0.59 (2.2%)	1.5 (3.7%)	1.7 (2.2%)	1.4 (1.8%)
B	0.47 (1.6%)	1.4 (3.3%)	1.4 (1.9%)	1.2 (1.7%)
C	0.73 (2.5%)	2.0 (4.8%)	2.5 (3.2%)	2.0 (2.8%)
D	0.49 (1.6%)	1.4 (3.2%)	1.3 (1.7%)	1.3 (1.9%)
NF	0.48 (1.7%)	1.1 (2.5%)	2.3 (2.8%)	0.90 (1.1%)

this line-of-sight view, the average NF spray plumes have less interaction with another and remain more distinct from the injector tip to the plume tips. This agrees well with the previous analysis of Figure 9 and further exhibits the degree to which turbulence affects the plume-to-plume interaction as well as spray collapse.

Further quantification of spray parameters can provide further evidence of the impact of intake flow on spray morphology. Figure 13 shows the average axial penetration L derived from the binarization of the liquid spray. Table 4 shows the sample standard deviations for L and the opening spray angle α (Figure 14) at the middle and end of liquid injection. Despite the appearance of similar morphology for B and D in Figure 11, here it is obvious that with increasing in-cylinder velocity and decreasing bulk gas density, the penetration increases. This is unsurprising, since a higher bulk gas density means a higher amount of drag acting against the spray, while higher velocities work in an opposite way, facilitating penetration and decreasing the spray angle. The effects of flow dynamics on the penetration is even more evident by the addition of the NF case, which is a comparison that isolates the effects of the flow on the spray since the density is nearly atmospheric for cases A, C, and NF. In addition, for

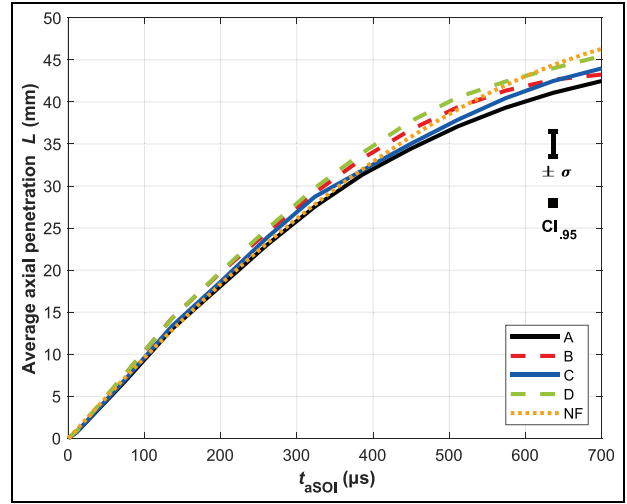


Figure 13. Average axial liquid penetration L . The interval given by the sample standard deviation σ (cf. Table 4) and the student- t 95 %-confidence interval ($CI_{.95}$) of the mean are plotted as an example for case A at $t = 636.2 \mu\text{s}$.

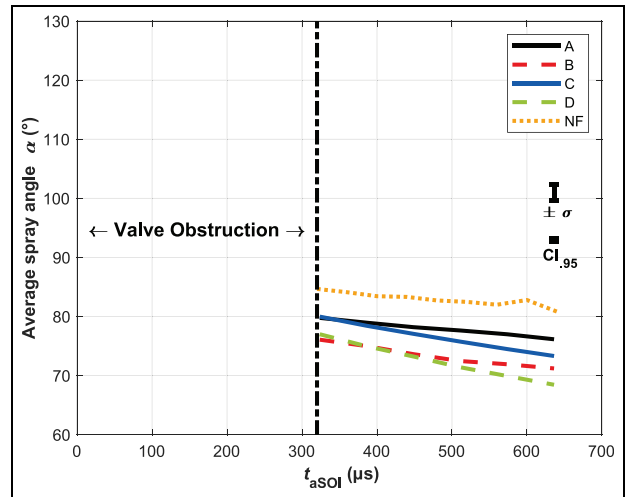


Figure 14. Average global spray angle α . The interval given by the sample standard deviation σ (cf. Table 4) and the student- t 95 %-confidence interval ($CI_{.95}$) of the mean are plotted as an example for case A at $t = 636.2 \mu\text{s}$.

cases of lower intake pressure, the liquid penetrations are similar until the later stages of injection. However, for OC A and C this is not necessarily true as the slope of the penetration length curve for C appears to fluctuate until the later stages of injection; whereas for A, the curve remains smooth. Furthermore, the slope of case B seems to taper off toward the end of the injection event, while the rest have similar slopes at the end. This phenomenon is likely explained by the rate of evaporation of case B shown in Figure 7, in which the evaporation rate during injection is the greatest of all cases.

The average global spray angle α is shown in Figure 14. As with penetration length, spray angle has clear relationships with bulk gas density and in-cylinder

flows. In the presence of decreasing bulk gas density, α also decreases. While Spray G2 (flash boiling) is not exactly achieved in this study due to the lower fuel temperature, lower α with lower intake pressure trends toward the principles of flash boiling, which causes total collapse, since the inner-spray recirculation is blocked by a pronounced plume-to-plume interaction.²² Yet, with higher in-cylinder speeds, the spray also has a lower spray angle, which follows the trend shown by increasing L with increasing in-cylinder velocity. Combining these phenomena, a common trend emerges: the bulk spray morphology is heavily shaped by the in-cylinder flow since the downward flow acts in the same direction as the incoming spray, rather than opposing it. The enhancement of the spray penetration due to the downward and rightward-directed intake flow is the opposite trend as is present in the case of late injection, where the bulk gas motion is pointed upward with the compressing piston, and this motion inhibits the downward spray penetration while simultaneously preventing spray collapse.²⁴ In the case of late injection, however, a trade-off exists which places the desired increased spray stability at increasing engine speed against the unacceptable increase of wall wetting as the spray comes into contact with the piston surface earlier and therefore, longer. Therefore, for future Spray G investigations, in light of a trend toward decreased spray stability with increasing in-cylinder velocities, there is much to be gained in further examining the early injection cases.

Conclusions

Through the use of PIV and volumetric Mie scatter imaging, the effects of in-cylinder flow velocity and bulk gas density were investigated for early injection Spray G conditions in an optical research engine. Extending the available research of early injection Spray G from generic test cases in constant volume chambers and bottom-view spray morphology investigations in more realistic engine conditions,²³ this work provides a more complete characterization of the spray morphology and the blueprint for future investigations to help increase efficiency and reduce emissions in DISI engine combustion through the following conclusions:

1. Turbulent kinetic energy k showed a high correlation between velocity magnitude and fluctuations; yet, the introduction of sprays during early injection did not generate more turbulence in the chosen region of interest long after injection. The lack of apparent added velocity fluctuations within the chosen region of interest (beginning 10 mm downstream of the injector tip) is probably due to the added turbulence being carried downward in the direction of the bulk flow out of the engine's optical access. The result that early injection does not increase k is supported by the findings of Chen et al.¹⁵ who found

that by the time of ignition, k was unchanged by the addition of an early injection from a multi-hole injector. Finally, the sprays themselves were shown to exhibit little variability, a phenomenon that may prevent greater k after injection. Regardless of the causes of little to no addition of k , in future investigations a longer injection duration or multiple injections would expand the data set of k to a larger range of conditions valuable to modern DISI operating strategies.

2. Wall wetting is clearly visible on the spark plug in this engine configuration and evidence strongly suggests that the spray interacts significantly with the intake valves. It is also plausible that wall wetting occurs on the cylinder walls as well as the piston surface, especially given a longer injection duration. While it is difficult to quantify wall wetting on all surfaces in such a complex engine experiment, future experiments could utilize well-known methods such as LIF or refractive index matching (RIM) to measure the fuel film on the piston surface^{7,39} and investigate the effects of wall wetting with Spray G on engine performance and emissions.
3. With decreasing intake pressure (decreasing bulk gas density) and increasing engine speed (increasing in-cylinder velocity magnitude) a number of phenomena, which are not possible to observe in constant volume chambers, occur. First, evaporation occurs quicker in the low density environment and this is accelerated by increased convection and presumably mixing at increased velocities. Second, plume-to-plume interaction is increased, especially by increased intake velocities compressing the plumes in the direction of the exhaust valves. This leads to a decrease in spray angle α , especially at lower bulk densities. Third, a greater axial liquid penetration L occurs due to decreased drag, an effect of density, and a downward guiding motion due to the downward flow momentum.
4. Contrary to the case of late Spray G injection, early injection spray morphology is dominated by the downward (toward piston) and rightward (toward exhaust valves) bulk flow motion, which guides the spray further downward and pushes the spray toward the exhaust with increasing velocity. In the case of late injection Spray G, higher engine speeds act to prevent spray collapse; while in early injection cases the opposite effect occurs. The simplified engine no-flow case exemplified the influence of the intake flow motion on the spray shape in a more engine-relevant geometry by eliminating other factors such as dynamic components or variations in bulk gas density. In the complete absence of surrounding air motion, the spray exhibits an ideal, symmetric shape without much inter-plume interaction or collapse. Therefore, further studies should characterize the degree to which spray

stability is affected and what effect this has on combustion performance.

There is still much knowledge to be gained in simpler DISI configurations like the no-flow case of Experiment IV investigating direct injection within a flow bench. Such configurations can be used to bridge the complexity gap between CVC sprays and optical research engine sprays. With the help of advanced diagnostics and numerical simulations in simpler and increasingly realistic DISI configurations alike, future engines still employing combustion will continue to improve in efficiency and emissions.

Acknowledgements

The authors would like to thank the whole ECN for their support, in particular S. Parrish for modifying the injector, and L. Pickett and G. Bruneaux for fruitful discussions on the topic.





Declaration of conflicting interests

The author(s) declared no potential conflicts of interest with respect to the research, authorship, and/or publication of this article.

Funding

The author(s) disclosed receipt of the following financial support for the research, authorship, and/or publication of this article: Deutsche Forschungsgemeinschaft through SFB/Transregio 150 (project number 237267381-TRR150).

ORCID iDs

Cooper Welch  <https://orcid.org/0000-0001-9067-9405>
 Marius Schmidt  <https://orcid.org/0000-0002-5424-1251>
 Christopher Geschwindner  <https://orcid.org/0000-0001-7869-2682>
 Margaret S Wooldridge  <https://orcid.org/0000-0003-1754-180X>

References

- Heywood JB. *Internal combustion engine fundamentals*. 2nd ed. New York, NY: McGraw-Hill Education, 2018.
- Peterson B, Reuss DL and Sick V. High-speed imaging analysis of misfires in a spray-guided direct injection engine. *Proc Combust Inst* 2011; 33(2): 3089–3096.
- Fansler TD, Reuss DL, Sick V and Dahms RN. Invited review: combustion instability in spray-guided stratified-charge engines: a review. *Int J Engine Res* 2015; 16(3): 260–305.
- Zhao F, Lai MC and Harrington DL. Automotive spark-ignited direct-injection gasoline engines. *Prog Energy Combust Sci* 1999; 25(5): 437–562.
- Heywood JB. *Internal combustion engine fundamentals*. New York, NY: McGraw-Hill, 1988.
- Robert Bosch GmbH. *Bosch automotive handbook*. 7th ed. Gerlingen and Chichester: Robert Bosch GmbH and John Wiley, [distributor] 2007.
- Ding CP, Vuilleumier D, Kim N, Reuss DL, Sjöberg M and Böhm B. Effect of engine conditions and injection timing on piston-top fuel films for stratified direct-injection spark-ignition operation using e30. *Int J Engine Res* 2020; 21: 302–318.
- Lee Z, Kim D and Park S. Effects of spray behavior and wall impingement on particulate matter emissions in a direct injection spark ignition engine equipped with a high pressure injection system. *Energy Convers Manag* 2020; 213: 112865.
- Shahbaz MA, Jüngst N, Grzeszik R and Kaiser SA. Endoscopic fuel film, chemiluminescence, and soot incandescence imaging in a direct-injection spark-ignition engine. *Proc Combust Inst* 2021; 38: 5869–5877.
- Serras-Pereira J, Aleiferis P, Richardson D, et al. Spray development, flow interactions and wall impingement in a direct-injection spark-ignition engine. SAE paper 2007-01-2712, 2007.
- Marchi A, Nouri J, Yan Y and Arcoumanis C. Spray stability of outwards opening pintle injectors for stratified direct injection spark ignition engine operation. *Int J Engine Res* 2010; 11(6): 413–437.
- Stiehl R, Schorr J, Krüger C, Dreizler A and Böhm B. In-cylinder flow and fuel spray interactions in a stratified spray-guided gasoline engine investigated by high-speed laser imaging techniques. *Flow Turbul Combust* 2013; 91(3): 431–450.
- Stiehl R, Bode J, Schorr J, Krüger C, Dreizler A and Böhm B. Influence of intake geometry variations on in-cylinder flow and flow–spray interactions in a stratified direct-injection spark-ignition engine captured by time-resolved particle image velocimetry. *Int J Engine Res* 2016; 17(9): 983–997.
- Peterson B, Baum E, Ding CP, Michaelis D, Dreizler A and Böhm B. Assessment and application of tomographic piv for the spray-induced flow in an ic engine. *Proc Combust Inst* 2017; 36(3): 3467–3475.
- Chen H, Zhuang H, Reuss DL, et al. Influence of early and late fuel injection on air flow structure and kinetic energy in an optical sidi engine. SAE paper 2018-01-0205, 2018.
- Sharma N, Bachalo WD and Agarwal AK. Spray droplet size distribution and droplet velocity measurements in a firing optical engine. *Phys Fluids* 2020; 32(2): 023304.
- Engine Combustion Network. Gasoline spray combustion. <https://ecn.sandia.gov/gasoline-spray-combustion/> (2017, accessed 26 February 2019).
- Manin J, Jung Y, Skeen SA, et al. Experimental characterization of di gasoline injection processes. SAE paper 2015-01-1894, 2015.
- Payri R, Salvador FJ, Martí-Aldaraví P and Vaquerizo D. ECN spray g external spray visualization and spray collapse description through penetration and morphology analysis. *Appl Therm Eng* 2017; 112: 304–316.
- Lacey J, Poursadegh F, Brear MJ, et al. Generalizing the behavior of flash-boiling, plume interaction and spray collapse for multi-hole, direct injection. *Fuel* 2017; 200: 345–356.
- Montanaro A, Allocca L and Lazzaro M. Iso-octane spray from a gdi multi-hole injector under non- and flash boiling conditions. SAE paper 2017-01-2319, 2017.
- Sphicas P, Pickett LM, Skeen SA and Frank JH. Inter-plume aerodynamics for gasoline spray collapse. *Int J Engine Res* 2018; 19(10): 1048–1067.

23. Gutierrez L, Mansfield AB, Fatouraie M, et al. Effects of engine speed on spray behaviors of the engine combustion network “spray g” gasoline injector. SAE paper 2018-01-0305, 2018.
24. Geschwindner C, Kranz P, Welch C, et al. Analysis of the interaction of spray g and in-cylinder flow in two optical engines for late gasoline direct injection. *Int J Engine Res* 2020; 21(1): 169–184.
25. Paredi D, Lucchini T, D’Errico G, et al. Combined experimental and numerical investigation of the ECN spray g under different engine-like conditions. SAE paper 2018-01-0281, 2018.
26. Paredi D, Lucchini T, D’Errico G, Onorati A, Pickett L and Lacey J. Validation of a comprehensive computational fluid dynamics methodology to predict the direct injection process of gasoline sprays using spray g experimental data. *Int J Engine Res* 2020; 21(1): 199–216.
27. Pati A, Paredi D, Lucchini T and Hasse C. CFD modeling of gas-fuel interaction and mixture formation in a gasoline direct-injection engine coupled with the ECN spray g injector. SAE paper 2020-01-0327, 2020.
28. Baum E, Peterson B, Böhm B and Dreizler A. On the validation of les applied to internal combustion engine flows: part 1: comprehensive experimental database. *Flow Turbul Combust* 2014; 92(1-2): 269–297.
29. Freudenhammer D, Baum E, Peterson B, Böhm B, Jung B and Grundmann S. Volumetric intake flow measurements of an ic engine using magnetic resonance velocimetry. *Exp Fluids* 2014; 55(5): 1724.
30. Renaud A, Ding CP, Jakirlic S, Dreizler A and Böhm B. Experimental characterization of the velocity boundary layer in a motored ic engine. *Int J Heat Fluid Flow* 2018; 71: 366–377.
31. Bürkle S, Biondo L, Ding CP, et al. In-cylinder temperature measurements in a motored ic engine using tdlas. *Flow Turbul Combust* 2018; 101(1): 139–159.
32. Welch C, Schmidt M, Keskinen K, et al. The effects of intake pressure on in-cylinder gas velocities in an optically accessible single-cylinder research engine. SAE paper 2020-01-0792, 2020.
33. Hamzah A, Poursadegh F, Lacey J, et al. A comparison of diffuse back-illumination (dbi) and mie-scattering technique for measuring the liquid length of severely flashing spray. In: *Proceedings of the 20th Australasian fluid mechanics conference*, Perth, Australia, 5–8 December 2016. <https://people.eng.unimelb.edu.au/imarusic/proceedings/20/669%20Paper.pdf>
34. Haussmann M, Ries F, Jeppener-Haltenhoff JB, et al. Evaluation of a near-wall-modeled large eddy lattice boltzmann method for the analysis of complex flows relevant to ic engines. *Computation* 2020; 8(2): 43.
35. Wieneke B. Piv uncertainty quantification from correlation statistics. *Meas Sci Technol* 2015; 26(7): 074002.
36. Pope SB. *Turbulent flows*. Cambridge: Cambridge University Press, 2012.
37. Zeng W, Sjöberg M, Reuss DL and Hu Z. The role of spray-enhanced swirl flow for combustion stabilization in a stratified-charge disi engine. *Combust Flame* 2016; 168: 166–185.
38. Aleiferis PG and Behringer MK. Modulation of integral length scales of turbulence in an optical si engine by direct injection of gasoline, iso -octane, ethanol and butanol fuels. *Fuel* 2017; 189: 238–259.
39. Drake MC and Haworth DC. Advanced gasoline engine development using optical diagnostics and numerical modeling. *Proc Combust Inst* 2007; 31(1): 99–124.